Bifurcations and interacting modes in coupled lasers: A strong-coupling theory

Sebastian Wieczorek and Weng W. Chow
Semiconductor Material and Device Sciences Department, Sandia National Laboratories, Albuquerque, New Mexico 87185-0601, USA
(Received 4 August 2003; revised manuscript received 21 October 2003; published 18 March 2004)

The paper presents a theoretical study of synchronization between two coupled lasers. A theory valid for arbitrary coupling between lasers is used. Its key feature is that the laser field is decomposed in terms of the composite-cavity modes reflecting the spatial field dependence over the entire coupled-laser system. The ensuing multimode equations are reduced to class-*B*, and further to class-*A* equations which resemble competing species equations. Bifurcation analysis, supported by insight provided by analytical solutions, is used to investigate influences of pump, carrier decay rate, polarization decay rate, and coupling mirror losses on synchronization between lasers. Population pulsation is found to be an essential mode competition mechanism responsible for bistability in the synchronized solutions. Finally, we discovered that the mechanism leading to laser synchronization changes from strong composite-cavity mode competition in class-*A* regime to frequency locking of composite-cavity modes in class-*B* regime.

DOI: 10.1103/PhysRevA.69.033811 PACS number(s): 42.55.Ah, 05.45.Xt, 02.30.Oz

I. INTRODUCTION

The first observation of light amplification by stimulated emission of radiation took place in 1960 [1]. Soon after, lasers became sufficiently reliable for scientists to consider coupling and synchronizing two lasers [2–4]. These inquires were driven by purely academic interest as well as by exciting applications. A single unperturbed laser can be viewed as a paradigm of synchronization. It works because all the atoms in the active medium are fully synchronized, they oscillate in-phase and produce coherent radiation. An interesting question arises about the conditions under which two different sets of synchronized atoms can synchronize with each other. Synchronized lasers are desired for a wide range of applications, such as frequency stabilization against cavity-length fluctuations [5,6], high power operation [7–10], and selective mode suppression [11].

The first theories of coupled lasers were proposed by Basov *et al.* [2], Perel and Rogova [3], and Spencer and Lamb [4]. They derived equations for the electric-field intensity and phase in each individual laser and found that coupled lasers may synchronize, i.e., lase at the same frequency despite differences in resonator lengths. Since then, coupled lasers remain an intensively studied problem for which several models were proposed. The early studies were concerned with synchronization between two gas lasers [12–15]. As this research was continued [16–25] some investigators tried to understand systems of three coupled lasers [26,27] and even large arrays of solid-state lasers [28–31]. In the late 1980's the focus shifted towards coupled semiconductor lasers [32–38] and semiconductor laser arrays [39–48]. At present, linear semiconductor laser arrays constitute the only commercially available coupled lasers.

Besides continuous wave operation, coupled lasers often show complicated dynamical behavior and instabilities. Among the recent studies of coupled lasers are those involving synchronization of coupled-chaotic lasers [26,49–52], and large arrays of nonidentical lasers [53]. In particular, studies of chaotic synchronization, with a significant contribution from the laser field [49,50], gave a more general meaning to the word ''synchronization'' which was originally used to describe synchronized periodic oscillators.

An important aspect of coupled laser theories is the description of the laser field and its interaction with the active medium. In the framework of a semiclassical approach, the laser medium is described quantum mechanically and the laser field is described classically [54]. The theory results in equations of motion for the intracavity electric field, active medium polarization and population inversion. In general, these quantities are functions of both space and time, whose dynamics are governed by partial differential equations (PDEs). In particular, the laser field equation is an inhomogeneous wave equation that is derived from Maxwell's equations by assuming that the effects of the active medium may be represented by a macroscopic polarization. Different methods exist for solving the PDEs; see the examples of treating external cavity lasers [55,56], multisection DFB lasers [57,58], and coupled multimode lasers [59].

The solution of PDEs is often numerically demanding, and more importantly in our case, not well suited for bifurcation analysis. Fortunately, simpler models, which are still based on semiclassical laser theory, have been developed. A widely used approach involves solving the inhomogeneous wave equation by expanding the laser field as a linear superposition of the solutions of the homogeneous wave equation. These solutions are commonly referred to as the passive-cavity eigenmodes. The expansion coefficients (electric-field amplitudes), which depend only on time, are then governed by ordinary differential equations (ODEs).

There are two approaches to treating the passive-cavity mode aspect of the coupled-laser problem. The more common approach neglects the effects of coupling between the resonators when solving the homogenous wave equation. The solutions are then simply the passive-cavity eigenmodes of the individual uncoupled resonators, and the contributions from resonator coupling are transferred to the inhomogeneous wave equation [36,41,52]. Basically, the laser field amplitude equations consist of the free-running laser contributions, together with terms describing the presence in the cavity of a small portion of fields from neighboring lasers.

When combined with the appropriate active medium description, the approach has been demonstrated to accurately reproduce experimental results under special conditions [52,60,61]. In addition, it has the advantage of flexibility, in terms of readily allowing the introduction of delay in the coupling fields [48], and global coupling via interaction of individual lasers with a mean field [53]. A serious concern is the ability of a field expansion in terms of uncoupled laser modes to accurately describe situations other than those involving weakly coupled lasers.

The second approach to treating the passive-cavity problem involves solving the homogeneous wave equation in the presence of resonator coupling. Since the solutions are the eigenmodes of the entire coupled-resonator system, they are often referred to as the passive composite-cavity modes [12–14] or supermodes [39]. There are several advantages to using the composite-resonator mode approach. The most important is that the description is valid for arbitrary coupling: from zero coupling, where the composite-cavity modes are the modes of the individual resonators, to maximum coupling, where the composite-cavity modes are the modes of a single resonator that has the combined volume of the two lasers. In particular, the dependences of eigenfrequencies and eigenfunctions on coupling between cavities are precisely determined (see Fig. 2). Such a feature is, of course, not present when the field expansion is in terms of uncoupled-individual-cavity modes. Another advantage is that the inhomogeneous wave equation, which governs the time evolution of the electric field amplitudes for composite-resonator modes, takes the form of that for the familiar multimode single-resonator laser. Thus one benefits from previously developed techniques and concepts, especially those relating to mode competition and locking. Furthermore, with the resulting numerical model described entirely by differential algebraic equations (DAEs), the numerics are less computer resource demanding and bifurcation analysis becomes possible. The third advantage involves physical properties of the coupled-laser system that are sensitive to spatial field variations. The description of such properties, e.g., coupling mirror losses, are more accurate and straightforward in terms of composite-cavity eigenmodes.

Owing to the above advantages, we choose to work with the composite-cavity mode approach in this paper. The inhomogeneous wave equation, in the slowly varying amplitude and phase approximation, can then be written as a set of coupled ODEs, describing the time evolution of the composite-cavity mode amplitudes and phases. Each equation contains a driving term that is due to the active medium polarization. The next step in the development of a coupled-laser theory is the derivation and solution of the quantum-mechanical equations of motion for the polarization and population. Two levels of approximations exist for the treatment of these equations. They involve the adiabatic elimination of the polarization equation (class-*B* lasers), and elimination of both the polarization and population equations (class-*A* lasers). Both cases are considered in this paper.

The final and perhaps most important step in our study is the introduction of the modern tools from bifurcation theory into the framework of the microscopic coupled-laser theory. Essentially, these techniques [62] allow swift continuation (in a two-dimensional parameter plane) of the transitions between qualitatively different types of dynamical behavior, including unstable states. As a result, we can be more certain that interesting, or possibly different physical phenomena associated with coexisting attractors, saddle points and global bifurcations, are not overlooked, as would likely be the case in traditional analyses. Incorporating our DAEs into bifurcation-continuation techniques [62] allows for systematic and extensive analysis of synchronization (locking) and instabilities in coupled lasers. Consequently, one obtains a more complete understanding of the physics underlying coupled-cavity laser behavior, and in terms of device design, the capability for optimization studies over a considerably broader parameter space than previously possible.

Sections II A and II B review the laser theory based on passive composite-cavity modes. The treatment of the active medium is discussed in Secs. II C 1 and II C 2. Section II C 2 also shows that in the class-*A* approximation, analytic solutions exist, which give invaluable insight to numerical results. The remainder of the paper is devoted to using bifurcation theory with the microscopic coupled-laser theory to study coupled-laser behavior. In Sec. III, we consider the case of single-frequency synchronization (locking) between two end-to-end coupled lasers, and systematically study the influences of population pulsations and coupling mirror losses on the lockband. We define the lockband as the range of cavity detuning within which the two coupled lasers are locked: operate with the same frequency. The results are first presented for class-*A* lasers, where the synchronization mechanism is the competition between composite-cavity modes. Then we discuss the transition from class-*A* to class-*B* equations. Here, bifurcation theory shows a qualitative change in the physical mechanism responsible for the transition between locked and unlocked lasers. In class-*B* lasers, the synchronization mechanism changes to frequency locking of the composite-cavity modes. The transition to class-*B* lasers is the starting point for investigating the important and more complicated class of coupled semiconductor lasers.

II. THEORY

The description of the coupled-laser model is divided into three parts. In the first part we describe passive (empty) composite-cavity modes and derive equations which determine the eigenfrequencies and eigenfunctions. In the second part, the equations for the time evolution of the electric-field amplitude and phase associated with a particular composite-cavity mode are derived from Maxwell equations. Furthermore, the equations describing the time evolution of the polarization and population inversion in a two-level medium are derived from quantum mechanics. In the third part, we show the reduction of the full set of equations by adiabatic elimination of polarization and population difference.

A. Composite-cavity modes

The wave equation

$$\nabla^2\vec{\mathcal{E}}-\frac{\epsilon_b(\vec{r})}{c^2}\ddot{\vec{\mathcal{E}}}-\mu_0\sigma\ \dot{\vec{\mathcal{E}}}=\mu_0\ \ddot{\vec{\mathcal{P}}}+\vec{\nabla}(\vec{\nabla}\cdot\vec{\mathcal{E}}), \qquad (1)$$

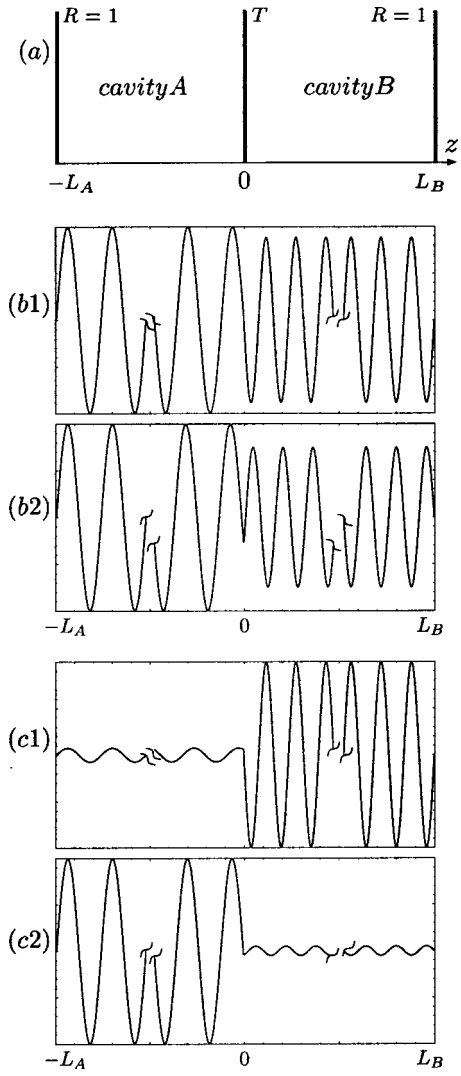

FIG. 1. Two resonators with $n_A=1$, $n_B=1.5$, and $L_A/\lambda=10^6$ coupled by a common coupling mirror of transmission T (a). Panels (b) show the antisymmetric (out-of-phase) (b1) and the symmetric (in-phase) (b2) composite-cavity mode in the strong-coupling region of $T=0.1$ and $dL/\lambda=0.01$. Panels (c) show the antisymmetric (out-of-phase) (c1) and the symmetric (in-phase) (c2) composite-cavity mode in the weak-coupling region of $T=0.01$ and $dL/\lambda=0.1$.

describes the propagation of the electric-field $\vec{\mathcal{E}}$ (in a medium with the dielectric constant $\epsilon_b(\vec{r})$ and conductivity σ) driven by the field-induced polarization $\vec{\mathcal{P}}$; $c=1/\sqrt{\epsilon_0\mu_0}$ is the speed of light in the vacuum. For the transversal field, $\vec{\nabla}(\vec{\nabla}\cdot\vec{\mathcal{E}})=\vec{0}$. In a passive cavity ($\vec{\mathcal{P}}=\vec{0}$) without losses ($\sigma=0$) and under the assumption that the electric-field varies along the longitudinal z direction only, we get

$$\frac{\partial^2}{\partial z^2}\mathcal{E}(z,t)=\mu_0\epsilon_0\,\epsilon_b(z)\frac{\partial^2}{\partial t^2}\mathcal{E}(z,t). \tag{2}$$

Following Spencer and Lamb [4], we define for the coupled-cavity structure in Fig. 1(a) the background dielectric constant

$$\epsilon_b(z)=\Theta(-L_A,0)\,\epsilon_b^A+\Theta(0,L_B)\,\epsilon_b^B+\frac{\eta}{k}\,\delta(z), \tag{3}$$

where for $x_1\leqslant x_2$ we define the rectangular function

$$\begin{aligned}\Theta(x_1,x_2)&=1 \quad \text{for} \quad x_1<x<x_2,\\ \Theta(x_1,x_2)&=0 \quad \text{for} \quad x_1>x>x_2.\end{aligned} \tag{4}$$

$\delta(z)$ is the Dirac delta function, and $k=\Omega/c$ is the wave vector in vacuum. The coupling mirror of transmission T is modeled as a dielectric ''bump'' with a coupling coefficient η given by

$$\eta=(n_A+n_B)\sqrt{\frac{1-T}{T}}. \tag{5}$$

The electric-field with amplitude $\mathcal{E}_0$ and associated with a passive composite-cavity eigenmode

$$\mathcal{E}(z,t)=\mathcal{E}_0 u(z)\exp(-i\Omega t)+\text{c.c.}, \tag{6}$$

is substituted into Eq. (2) to yield the equation for an eigenfunction $u(z)$

$$\frac{d^2}{dz^2}u(z)=-\mu_0\,\epsilon_0\epsilon_b(z)\Omega^2\,u(z). \tag{7}$$

As shown in Refs. [4,14], each eigenfunction satisfies the boundary conditions

$$\frac{d}{dz}u(0^+)-\frac{d}{dz}u(0^-)=-k\eta\,u(0), \tag{8}$$

$$u(0^+)=u(0^-), \tag{9}$$

$$u(-L_A)=u(L_B)=0., \tag{10}$$

where 0^+ and 0^- denote positions infinitesimally before and after the coupling mirror, and $z=-L_A, L_B$ are the end mirror positions.

The nth mode solution of Eq. (8) satisfying the boundary conditions (8)–(10) is

$$\begin{aligned}u_n(z)&=A_n\sin[k_n n_A(z+L_A)] \quad \text{for} \quad -L_A\leqslant z\leqslant 0,\\ u_n(z)&=B_n\sin[k_n n_B(z-L_B)] \quad \text{for} \quad 0\leqslant z\leqslant L_B.\end{aligned} \tag{11}$$

The eigenmodes obey the orthogonality relation

$$\int_{-L_A}^{L_B} dz\;\epsilon_b(z)\,u_n(z)u_m(z)=\mathcal{N}\delta_{nm}, \tag{12}$$

where $\mathcal{N}$ is the normalization constant. From the orthogonality relation we get

$$A_n^2 n_A^2 L_A\left(\frac{1}{2}-\frac{\sin(2k_n n_A L_A)}{4k_n n_A L_A}\right)\sqrt{T}+B_n^2 n_B^2 L_B \times\left(\frac{1}{2}-\frac{\sin(2k_n n_B L_B)}{4k_n n_B L_B}\right)\sqrt{T} +A_n^2\frac{(n_A+n_B)}{k_n}\sin^2(k_n n_A L_A)\sqrt{1-T}=\mathcal{N}\sqrt{T} \tag{13}$$

which needs to be solved simultaneously with the boundary conditions (8) and (9):

$$\sqrt{T}[B_n n_B\cos(k_n n_B L_B)-A_n n_A\cos(k_n n_A L_A)] =-\sqrt{1-T}A_n(n_A+n_B)\sin(k_n n_A L_A), \tag{14}$$

and

$$A_n\sin(k_n n_A L_A)=-B_n\sin(k_n n_B L_B), \tag{15}$$

to obtain the wave vectors k_n and the corresponding composite-mode amplitudes A_n and B_n. More generally, this can be done for any number m of coupled lasers where one has to solve $m+1$ algebraic equations to determine the composite-cavity modes [12].

In the remaining part of this manuscript we are concerned with coupled lasers hosting the same type of an active medium $\epsilon_b=\epsilon_b^A=\epsilon_b^B$. Furthermore, we choose $\mathcal{N}=\epsilon_b L$, where $L=L_A\approx L_B$, and introduce the relative length difference

$$\frac{dL}{\lambda}=\frac{L_B-L_A}{\lambda}, \tag{16}$$

where $\lambda=1\ \mu m$ is approximately the wavelength of the free-running single laser.

Four examples of calculated composite-cavity modes are plotted in Figs. 1(b) and 1(c). In the region of strong coupling, as shown in panel (b), composite-cavity eigenmodes have roughly similar amplitudes in both cavities. Furthermore, solutions of Eq. (15) can be described as *antisymmetric* (b1) and *symmetric* (b2). These names refer to the fact that, at the end mirrors, the field of the symmetric modes is in phase while the field of the antisymmetric modes is π out of phase. Panels (c1) and (c2) show the antisymmetric and the symmetric modes, respectively, in the region of weak coupling. As the coupling decreases to zero, we find that the symmetric modes reside in cavity A and the antisymmetric modes reside in cavity B for $L_A<L_B$, and otherwise for $L_A>L_B$.

In Fig. 2, we plot some solutions of Eq. (15) as a function of the coupling mirror transmission T. The eigenmode wave vectors were assigned the labels a for antisymmetric and s for symmetric. For small values of dL/λ and T the symmetric and the antisymmetric solutions, namely $k_{s\pm n}$ and $k_{a\pm n}$, stay close to each other as compared to the distance between $k_{a(s)\pm n}$ and $k_{a(s)\pm(n\pm1)}$. When dL/λ reaches the value 0.25 all the modes become equidistant, and as dL/λ approaches 0.5 they again resemble the situation for $dL/\lambda=0.05$ except

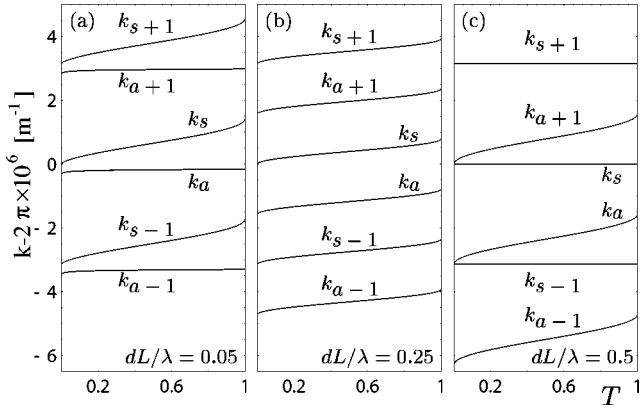

FIG. 2. Evolution of the composite-mode wave numbers k_x [solutions of the transcendental equation (14)] with increasing T. From (a) to (c) dL/λ takes values: 0.05, 0.25, and 0.5 while $L_A/\lambda=10^6$.

that $k_{s\pm n}$ takes place of $k_{a\pm n}$. Here, we focus our attention on the interaction between the two modes, denoted as k_a and k_s in Fig. 2, so we consider the range $-0.25\leqslant(dL/\lambda)\leqslant0.25$

Lastly, we note that the assumption of perfectly reflecting end mirrors is an idealization used to obtain normal composite-cavity eigenmodes. This assumption is valid, for example, in coupled VCSEL's [10] and low-gain lasers. When outcoupling losses become significant, the more complicated nonorthogonal eigenmodes should be considered [63,64].

B. Laser equations

In this section, we are concerned with the time evolution of (i) the real electric-field amplitude $E_n(t)$ and phase $\phi_n(t)$ associated with the nth composite-cavity eigenmode, (ii) the corresponding complex polarization amplitudes $\mathcal{P}_n(t)$, and (iii) the population inversion $N_{A(B)}$ in cavities A and B. We rewrite Eq. (1) in the form

$$\left(-\frac{\partial^2}{\partial z^2}+\frac{\epsilon_b(z)}{c^2}\frac{\partial^2}{\partial t^2}+\mu_0\sigma\frac{\partial}{\partial t}\right)\mathcal{E}(z,t)=-\mu_0\frac{\partial^2}{\partial t^2}\mathcal{P}(z,t), \tag{17}$$

where the electric-field losses $\Gamma_E=\sigma/(\epsilon_0\epsilon_b)$ are

$$\Gamma_E(z)=\Gamma_{out}+\Gamma_M L\,\delta(z)=-\frac{c}{2(L_A+L_B)}\ln(R_1R_2) +\Gamma_M L\,\delta(z), \tag{18}$$

where Γ_{out} accounts for the outcoupling losses, R_1 and R_2 are the end mirrors reflectivities, and Γ_M accounts for the absorption or scattering at the coupling mirror. The total electric field $\mathcal{E}(z,t)$ and the total macroscopic polarization $\mathcal{P}(z,t)$ are expanded in terms of the composite-cavity eigenmodes

$$\mathcal{E}(z,t)=\frac{1}{2}\sum_m \{E_m(t)\exp[-i(\nu_m t+\phi_m(t))]\,u_m(z)+\text{c.c.}\}, \tag{19}$$

and

$$\mathcal{P}(z,t)=\frac{1}{2}\sum_m \{\mathcal{P}_m(t)\exp[-i(\nu_m t+\phi_m(t))]\,u_m(z)+\text{c.c.}\}, \tag{20}$$

where $E_m(t)$ and $\phi_m(t)$ are the real, slowly varying, electric-field amplitude and phase of the mth mode, and $\mathcal{P}_m(t)$ is the corresponding complex, slowly varying, polarization amplitude.

1. Electric field

Substituting Eqs. (19) and (20) into Eq. (17) (see Ref. [54], p. 100) we arrive at the self-consistency equations

$$\dot{E}_n=-\frac{1}{2}(C_{nn}\Gamma_{out}+u_n^2(0)\Gamma_M)-\frac{\nu_n}{2\epsilon_0\epsilon_b}C_{nn}\,\mathrm{Im}(\mathcal{P}_n), \tag{21}$$

$$\dot{\phi}_n=\Omega_n-\nu_n-\frac{\nu_n}{2\epsilon_0\epsilon_b}C_{nn}\frac{\mathrm{Re}(\mathcal{P}_n)}{E_n}, \tag{22}$$

where the self-consistency arises from demanding that the electric field, inducing the active medium polarization, equals the field resulting from the induced polarization. As a consequence of the composite-cavity configuration, we have the modal integrals

$$C_{nm}=\frac{\epsilon_b}{\mathcal{N}}\int_{-L_A}^{L_B}dz\,u_n(z)u_m(z)=C_{nm}^A+C_{nm}^B, \tag{23}$$

$$C_{nm}^A=\frac{1}{2L}A_nA_m\left(\frac{\sin[(k_n-k_m)n_AL_A]}{(k_n-k_m)n_A}-\frac{\sin[(k_n+k_m)n_AL_A]}{(k_n+k_m)n_A}\right), \tag{24}$$

$$C_{nm}^B=\frac{1}{2L}B_nB_m\left(\frac{\sin[(k_n-k_m)n_BL_B]}{(k_n-k_m)n_B}-\frac{\sin[(k_n+k_m)n_BL_B]}{(k_n+k_m)n_B}\right). \tag{25}$$

In a long (compare to the wavelength λ) cavity, $C_{n\neq m}$ is almost zero and C_{nn} is close to unity.

2. Active medium

In semiclassical laser theory, the macroscopic polarization $\mathcal{P}(r,t)$ of a two-level medium is given by

$$\mathcal{P}(z,t)=D(z)\,\mu_{ab}\,\rho_{ab}(z,t)+\text{c.c.}, \tag{26}$$

where μ_{ab} is the dipole matrix element, ρ_{ij} is the matrix element of the population operator (see Ref. [54], p. 103), and the local density of atoms is

$$D(z)=\Theta(-L_A,0)D_A+\Theta(0,L_B)D_B. \tag{27}$$

These matrix elements evolve accordingly to

$$\dot{\rho}_{ab}(z,t)=-i\omega\,\rho_{ab}(z,t)-\Gamma\rho_{ab}(z,t)+\frac{i\,\mu_{ab}}{\hbar}\mathcal{E}(z,t)\times[\rho_{bb}(z,t)-\rho_{aa}(z,t)], \tag{28}$$

$$\dot{\rho}_{aa}(z,t)=\Lambda_a(z)-\Gamma_a\rho_{aa}(z,t)-\frac{i\,\mu_{ab}}{\hbar}\mathcal{E}(z,t)\times[\rho_{ab}(z,t)-\rho_{ba}(z,t)], \tag{29}$$

$$\dot{\rho}_{bb}(z,t)=\Lambda_b(z)-\Gamma_b\rho_{bb}(z,t)+\frac{i\,\mu_{ab}}{\hbar}\mathcal{E}(z,t)\times[\rho_{ab}(z,t)-\rho_{ba}(z,t)], \tag{30}$$

where $\Gamma=\frac{1}{2}(\Gamma_a+\Gamma_b)+\Gamma_{dephase}$ is the polarization decay rate, $\Gamma_{dephase}$ includes dephasing effects due to elastic collisions, $\Lambda_a(z)$ and $\Lambda_b(z)$ are the pump rates into levels a and b, respectively, while Γ_a and Γ_b are the decay rates from levels a and b, respectively.

Identifying the positive-frequency parts in Eqs. (26) and (20)

$$D(z)\,\mu_{ab}\rho_{ab}(z,t)=\tfrac{1}{2}\sum_k\,\mathcal{P}_k(t)u_k(z)\exp(-i\psi_k), \tag{31}$$

where $\psi_k=\nu_k t+\phi_k$ is the total phase of the kth mode, we find that the kth mode of complex, slowly varying polarization

$$\mathcal{P}_k(t)=\mathcal{P}_k^A(t)+\mathcal{P}_k^B(t)=\frac{2}{\mathcal{N}}\exp(i\psi_k)\int_{-L_A}^{L_B}dz\,u_k(z)\epsilon_b(z)\,D(z)\mu_{ab}\rho_{ab}(z,t), \tag{32}$$

has its source in oscillating dipoles within cavities A and B

$$\mathcal{P}_k^{A(B)}(t)=\frac{2}{\mathcal{N}}\exp(i\psi_k)\mu_{ab}\epsilon_b^{A(B)}\rho_{ab}^{A(B)}(t)\int_{-L_A(0)}^{0(L_B)}dz\,u_k(z). \tag{33}$$

Combining time derivative of Eq. (32) with Eq. (28), defining population inversion in cavity $A(B)$ as $N_{A(B)}=D_{A(B)}(\rho_{aa}^{A(B)}-\rho_{bb}^{A(B)})$, gives time evolution for the kth mode of polarization

$$\mathcal{P}_k^{A(B)}=[i(\nu_k-\omega)-\Gamma]\mathcal{P}_k^{A(B)}-\frac{i\mu_{ab}^2}{\hbar}\times\sum_n\,E_n\exp(-i\psi_{nk})C_{kn}^{A(B)}N_{A(B)}, \tag{34}$$

where $\psi_{nk}=\psi_n-\psi_k$.

To obtain equations of motion for the population inversions $N_{A(B)}$, we multiply Eqs. (29) and (30) by $D(z)$, sub-

stitute Eq. (19), use Eq. (33), integrate over $(-L_A,0)$ and $(0,L_B)$ to distinguish between different cavities, and subtract the resulting equations for the density of electrons in levels a and b. This gives

$$\dot{N}_{A(B)}=\Lambda_{A(B)}-\Gamma_N N_{A(B)}+\frac{1}{\hbar}\sum_k E_k \mathrm{Im}(\mathcal{P}_k^{A(B)}), \quad (35)$$

where the pumping is $\Lambda_{A(B)}=(\Lambda_a^{A(B)}-\Lambda_b^{A(B)})D_{A(B)}$, and the population-difference decay rate is $\Gamma_N=\Gamma_a=\Gamma_b$.

C. Laser classes

The dynamics of a multimode double-cavity laser, in semiclassical theory, is fully described by Eqs. (21), (22), (34), and (35). If the decay rates Γ, Γ_E, and Γ_N are of similar magnitude all these equations are required to properly describe the laser dynamics. Such lasers, according to the notation introduced in Ref. [65], are called class-C lasers.

Trajectories of a single-mode class-C laser evolve in a four-dimensional phase space $\{E,N,\mathrm{Re}(\mathcal{P}),\mathrm{Im}(\mathcal{P})\}$ as shown in Fig. 3(a). However, most lasers are characterized by very short dephasing times, mostly due to elastic collisions, such that $\Gamma \gg \Gamma_E,\Gamma_N$ which allows the adiabatic elimination of $\mathcal{P}(t)$. When $\Gamma \gg \Gamma_E > \Gamma_N$, trajectories in the phase space rapidly approach the two-dimensional manifold defined by $\mathcal{P}=\mathcal{P}(E(t),N(t))$ and then evolve on this manifold as shown in Fig. 3(b). Such lasers belong to class B. When $\Gamma_E \ll \Gamma,\Gamma_N$, one can further reduce the system by eliminating population equation. These are class-A lasers and the electric-field alone is sufficient to describe their dynamics. For typical class-A lasers, $\Gamma > \Gamma_N$ and the trajectory rapidly converges to the two-dimensional manifold defined by $\mathcal{P}=\mathcal{P}(E(t),N(t))$ and, staying on this manifold, rapidly approaches the one-dimensional manifold defined by $N=N(E(t))$. Then, the trajectory slowly evolves along this one-dimensional manifold [Fig. 3(c)]. When $\Gamma \sim \Gamma_N$ one cannot distinguish the two steps in the fast approach towards the one-dimensional manifold.

In this paper, we first present a systematic study of synchronization in coupled-cavity lasers in class-A regime where we can derive analytical solutions for steady states and identify mechanisms for composite-cavity mode competition. Then, we study the transition from class A to class B. A systematic study of class-B lasers, which include the widely used semiconductor lasers, will be the subject of a later publication.

1. Class-B approximation

We multiply Eq. (35) by $\exp[-i(\nu_k-\omega)+\Gamma]t$ and integrate over the interval $(-\infty,t)$. Under the assumption $\Gamma \gg \Gamma_E,\Gamma_N$, the variables E, ϕ, and N vary little in the time Γ^{-1}, so that

$$\mathcal{P}_n=-\frac{i\mu_{ab}^2}{\hbar\Gamma}\sum_k E_k \exp(-i\,\psi_{kn})\mathcal{L}(\nu_k)(1-i\alpha_k) \times (C_{nk}^A N_A + C_{nk}^B N_B), \quad (36)$$

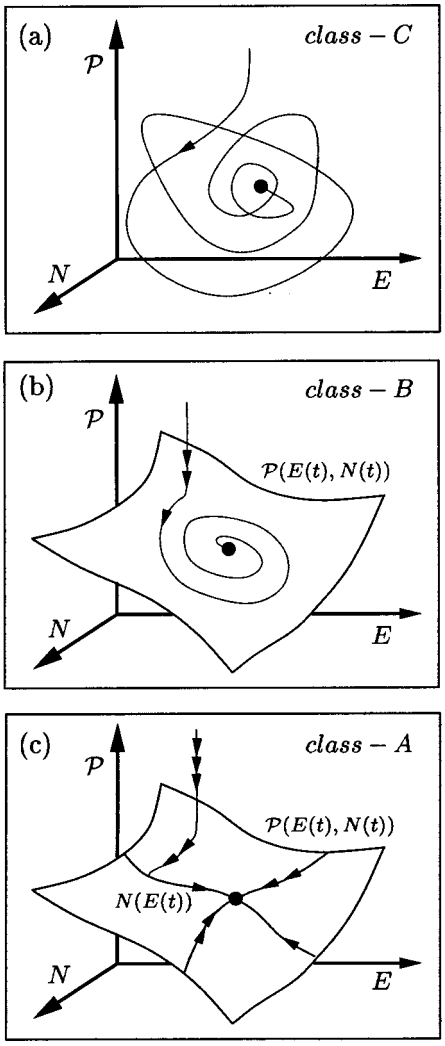

FIG. 3. Sketches of a typical trajectory approaching a stable fixed point in class-A, class-B, and class-C free-running lasers.

and

$$\mathcal{P}_n^{A(B)}=-\frac{i\mu_{ab}^2}{\hbar\Gamma}\sum_k E_k \exp[-i(\psi_{kn})]\mathcal{L}(\nu_k) \times (1-i\alpha_k)C_{nk}^{A(B)} N_{A(B)}, \quad (37)$$

where we introduced the Lorentzian

$$\mathcal{L}(\nu_n)=\frac{\Gamma^2}{\Gamma^2+(\omega-\nu_n)^2}, \quad (38)$$

and frequency pulling parameter

$$\alpha_n=\frac{\omega-\nu_n}{\Gamma}. \quad (39)$$

After substituting the imaginary part of Eq. (36) into Eq. (21), and the real part of Eq. (36) into Eq. (22), we obtain class-B field equations for the coupled lasers:

$$\dot{E}_n = -\frac{1}{2}\Gamma_E^n E_n + \frac{\mu_{ab}^2 \nu_n}{2\epsilon_0\epsilon_b \hbar\Gamma} C_{nn} \sum_k \mathcal{L}(\nu_k)[\cos(\psi_{kn}) - \alpha_k \sin(\psi_{kn})](C_{kn}^A N_A + C_{kn}^B N_B) E_k, \quad (40)$$

$$\dot{\phi}_n + \nu_n = \dot{\psi}_n = \Omega_n + \frac{\mu_{ab}^2 \nu_n}{2\epsilon_0\epsilon_b \hbar\Gamma} C_{nn} \sum_k \mathcal{L}(\nu_k)[\alpha_k \cos(\psi_{kn}) + \sin(\psi_{kn})](C_{kn}^A N_A + C_{kn}^B N_B)\frac{E_k}{E_n}, \quad (41)$$

where

$$\Gamma_E^n = C_{nn}\Gamma_{out} + u_n^2(0)\Gamma_M \quad (42)$$

represents the modal cavity losses. We recall that for a two-level (homogeneous) medium, frequencies of the modes are always pulled, due to α_k in Eq. (41), towards the center of the gain profile at ω.

Substituting the imaginary parts of Eq. (37) into Eq. (35), gives the class-B equations of motion for population in cavities A and B

$$\dot{N}_{A(B)} = \Lambda_{A(B)} - \Gamma_N N_{A(B)} - \frac{\mu_{ab}^2}{\hbar^2\Gamma} \sum_{m,n} C_{nm}^{A(B)} \mathcal{L}(\nu_m) E_m E_n \times [\cos(\psi_{mn}) - \alpha_m \sin(\psi_{mn})] N_{A(B)}. \quad (43)$$

Equation (43) includes some effects that are not present in a single-mode single-cavity laser. In multimode lasers there occurs an important effect of pulsation in population difference at the beat frequencies ψ_{nm}. This effect is called *population pulsation* and causes strong coupling between the modes [54,14]. Another important feature arises from the composite-cavity configuration. The factors $C_{nm}^{A(B)}$ (equal unity in single-cavity lasers) vary in coupled lasers with the detuning between cavities causing changes in mode competition.

To determine the modal gain $g_{nk} = g_{nk}^A + g_{nk}^B$ and gain-induced refractive index $\delta n_{nk} = \delta n_{nk}^A + \delta n_{nk}^B$, we use the definitions

$$\frac{d}{dt}E_n = -\frac{1}{2}\Gamma_E^n E_n + \frac{c}{n_b}\sum_k g_{nk} E_k \quad (44)$$

and

$$\frac{d}{dt}\phi_n = (\Omega_n - \nu_n) - \frac{\nu_n}{n_b}\sum_k \delta n_{nk}, \quad (45)$$

and extract from Eqs. (40) and (41)

$$g_{nk}^{A(B)}(\nu, N) = C_{nn} C_{kn}^{A(B)} \frac{\mu_{ab}^2 \nu_n}{2\, c\,\epsilon_0 n_b \hbar\Gamma} \mathcal{L}(\nu_k) \times [\cos(\psi_{kn}) - \alpha_k \sin(\psi_{kn})] N_{A(B)} \quad (46)$$

and

$$\delta n_{nk}^{A(B)}(\nu, N) = -C_{nn}\, C_{kn}^{A(B)} \frac{\mu_{ab}^2}{2\epsilon_0 n_b \hbar\Gamma} \mathcal{L}(\nu_k)[\alpha_k \cos(\psi_{kn}) + \sin(\psi_{kn})] N_{A(B)}, \quad (47)$$

so the nth mode frequency pulling parameter α_n becomes

$$\alpha_n = -\frac{\nu_n}{c}\frac{\delta n_{nn}}{g_{nn}}. \quad (48)$$

Because we have a multimode field, formulas (46) and (47) describe constant *diagonal terms* $(n=k)$ and oscillatory *off-diagonal terms* $(n\neq k)$. Furthermore, the expressions for g_{nk} and δn_{nk} consist of two types of contributions. One is the modal contribution represented by C_{nn} and $C_{nn}^{A(B)}$ that depends on the coupled-cavity configuration. In particular, integrals $C_{nn}^{A(B)}$ describe the overlap of the composite-cavity mode with the gain medium in cavity $A(B)$. The other is the local contribution that reflects the properties of the active medium. The local gain has the Lorentzian profile characteristic for homogeneously broadened media.

In terms of the modal gain (46) and the modal index change (47) , the population equation (43) becomes

$$\frac{d}{dt}N_{A(B)} = \Lambda_{A(B)} - \Gamma_N N_{A(B)} - \sum_{m,n} \frac{4\, g_{nm}^{A(B)}}{C_{nn}} \frac{I_{nm}}{\hbar\nu_n}, \quad (49)$$

where the effective electric-field intensity (in units of energy) is

$$I_{nm} = \tfrac{1}{2} c\,\epsilon_0 n_b E_n E_m. \quad (50)$$

The factor 4 in Eq. (49) appears because we deal with population-difference density. For semiconductor lasers, one considers the equation for the total carrier density in the conduction or valence band (Ref. [66], p. 47) in which case one gets a factor of 2 instead of 4.

Similarly, rewriting polarization (36)

$$\mathcal{P}_n = -\frac{2\epsilon_0\epsilon_b}{C_{nn}\nu_n}\sum_k \left(i\frac{c}{n_b}g_{nk} - \frac{\nu_n}{n_b}\delta n_{nk}\right)E_k \quad (51)$$

highlights the response of the active medium to a multimode electric field.

It is more convenient to work with the equations in a dimensionless form obtained by rescaling (i) the electric field E_k with respect to the electric field of the free-running single-cavity laser pumped twice above threshold, (ii) the population difference N with respect to its threshold value for the free-running single-cavity laser, and (iii) the time t with respect to Γ_N^{-1}. Using the new quantities

$$\tilde{E}_k = E_k\sqrt{\frac{\mu_{ab}^2}{\hbar^2\Gamma\Gamma_N}},\quad \tilde{N} = N\frac{\mu_{ab}^2\nu}{\epsilon_0\epsilon_b\hbar\Gamma\Gamma_E},$$

$$\tilde{t} = t\Gamma_N,\quad \tilde{\nu}_k = \frac{\nu_k}{\Gamma_N},\quad \tilde{\Omega}_k = \frac{\Omega_k}{\Gamma_N},$$

$$\tilde{\Lambda}_{A(B)}=\Lambda_{A(B)}\frac{\mu_{ab}^2\nu}{\epsilon_0\epsilon_b\hbar\Gamma\Gamma_E\Gamma_N},\quad \gamma=\frac{\Gamma_{out}}{2\Gamma_N},$$

$$\gamma_M=\frac{\Gamma_M}{\Gamma_{out}},\quad \text{and}\quad \gamma_n=\gamma[1+\gamma_M u_n^2(0)], \tag{52}$$

we rewrite Eqs. (40), (41), and (43)

$$\dot{\tilde{E}}_n=-\gamma_n\tilde{E}_n+\gamma C_{nn}\sum_k \mathcal{L}(\nu_k)[\cos(\psi_{kn})-\alpha_k\sin(\psi_{kn})]$$
$$\times(C_{kn}^A\tilde{N}_A+C_{kn}^B\tilde{N}_B)\tilde{E}_k, \tag{53}$$

$$\dot{\phi}_n+\tilde{\nu}_n=\dot{\psi}_n=\tilde{\Omega}_n+\gamma C_{nn}\sum_k \mathcal{L}(\nu_k)[\alpha_k\cos(\psi_{kn})+\sin(\psi_{kn})]$$
$$\times(C_{kn}^A\tilde{N}_A+C_{kn}^B\tilde{N}_B)\frac{\tilde{E}_k}{\tilde{E}_n}, \tag{54}$$

$$\dot{\tilde{N}}_{A(B)}=\tilde{\Lambda}_{A(B)}-\tilde{N}_{A(B)}-\sum_{m,n} C_{nm}^{A(B)}\mathcal{L}(\nu_m)\tilde{E}_m\tilde{E}_n$$
$$\times[\cos(\psi_{nm})+\alpha_m\sin(\psi_{nm})]\tilde{N}_{A(B)}, \tag{55}$$

where the derivatives are taken with respect to the new rescaled time $\tilde{t}$. This is the final form of the equations used for describing dynamics of class-*B* coupled-cavity multimode lasers with homogeneously broadened media.

Equations (53)–(55) for the pair of modes, denoted as k_s and k_a in Fig. 2, together with the mode equations (13)–(15) were used for all numerical calculations presented in Sec III. The complexity of these equations requires numerical analysis and, as a consequence, full physical understanding is sometimes difficult to achieve. An alternative is to start with the class-*A* approximation.

2. Class-A approximation

To illustrate the boundary between class-*A* and class-*B* lasers, we consider a coupled-laser system that is operating with a single composite-cavity mode, and use $C^A=C^B=\frac{1}{2}$ (equal cavity lengths). Then, Eqs. (53) and (55) take the form

$$\dot{\tilde{E}}=\gamma(\tfrac{1}{2}\tilde{N}-1)\tilde{E},$$

$$\dot{\tilde{N}}=\tilde{\Lambda}-\tilde{N}(1-\tfrac{1}{2}\tilde{E}^2), \tag{56}$$

where $\tilde{N}=\tilde{N}_A+\tilde{N}_B$ and $\tilde{\Lambda}=\tilde{\Lambda}_A+\tilde{\Lambda}_B$. At the fixed point $\tilde{E}=\sqrt{\tilde{\Lambda}-2},\tilde{N}=2$, a stability analysis gives the eigenvalues

$$\lambda_{1,2}=-\frac{\tilde{\Lambda}}{4}\pm\sqrt{\frac{\tilde{\Lambda}^2}{16}-\gamma(\tilde{\Lambda}-2)}. \tag{57}$$

If $(\tilde{\Lambda}^2/16)<\gamma(\tilde{\Lambda}-2)$, we have two complex conjugate eigenvalues and the fixed point is approached in the oscillatory fashion often called *relaxation oscillation*. On the other hand, if $(\tilde{\Lambda}^2/16)>\gamma(\tilde{\Lambda}-2)$ we have two real negative eigenvalues $\lambda_1\ll\lambda_2$ indicating that the dynamics can be reduced from two dimensions to only one dimension. The condition $(\tilde{\Lambda}^2/16)=\gamma(\tilde{\Lambda}-2)$, plotted in Fig. 4, defines the border between class-*B* lasers and class-*A* lasers. In class-*A* lasers, the population difference decays much faster then $\tilde{E}$ and can be adiabatically eliminated.

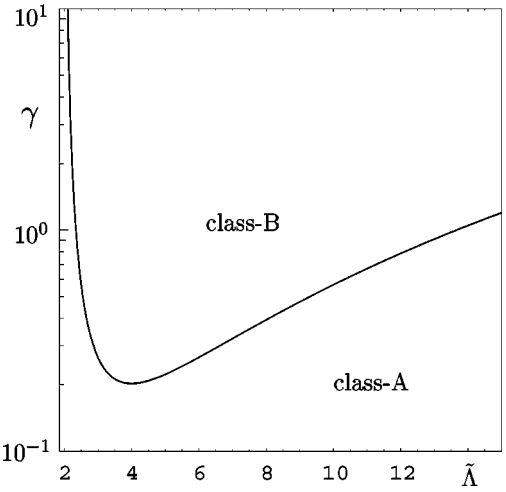

FIG. 4. The border between class-*A* and class-*B* regime for single-composite-mode coupled lasers where $\tilde{\Lambda}=\tilde{\Lambda}_A+\tilde{\Lambda}_B$.

There is a price to pay when eliminating population equation in a multimode theory. On the one hand, one can neglect the population pulsation terms in Eq. (55) and set the left hand side of Eq. (55) to zero. The resulting expression for $N_{A(B)}$ is valid for high pumping but does not include population pulsations. On the other hand, when the oscillatory terms in Eq. (55) are kept, one needs to use a perturbative approach. The resulting expression for $N_{A(B)}$ includes population pulsations but is valid only near threshold. Because population pulsations are important in our analysis we multiply Eq. (55) by e^t and formally integrate to obtain

$$\tilde{N}_{A(B)}=e^{-t}\int_{-\infty}^{t}\Big\{\tilde{\Lambda}_{A(B)}e^t-\sum_{m,n} C_{nm}^{A(B)}\mathcal{L}(\nu_m)\tilde{E}_m\tilde{E}_n$$
$$\times[\cos(\psi_{nm})+\alpha_m\sin(\psi_{nm})]\tilde{N}_{A(B)}(t)e^t\Big\}dt. \tag{58}$$

For $\tilde{E}_k=0$ one gets $\tilde{N}_{A(B)}^{(0)}=\tilde{\Lambda}_{A(B)}$. Using $\tilde{N}_{A(B)}(t)=\tilde{\Lambda}_{A(B)}$ in the right-hand side of Eq. (58), and assuming that $\tilde{E}_k$ and ϕ_k vary little during the time $\tilde{t}=1$ leads to

$$\tilde{N}_{A(B)}^{(2)}=\tilde{\Lambda}_{A(B)}-\tilde{\Lambda}_{A(B)}(C_{aa}^{A(B)}\mathcal{L}(\nu_a)\tilde{E}_a^2+C_{ss}^{A(B)}\mathcal{L}(\nu_s)\tilde{E}_s^2$$
$$+\tilde{E}_a\tilde{E}_sC_{as}^{A(B)}\mathcal{D}_{sa}\{w[d_{sa}\sin(\psi_{sa})+\cos(\psi_{sa})]$$
$$+v_{as}[\sin(\psi_{sa})-d_{sa}\cos(\psi_{sa})]\}), \tag{59}$$

where

$$d_{nm}=\frac{\nu_n-\nu_m}{\Gamma_N},\quad \mathcal{D}_{nm}=\frac{\Gamma_N^2}{\Gamma_N^2+(\nu_n-\nu_m)^2}, \tag{60}$$

and

$$w=\mathcal{L}(\nu_a)+\mathcal{L}(\nu_s),\quad v_{as}=\alpha_a\mathcal{L}(\nu_a)-\alpha_s\mathcal{L}(\nu_s). \tag{61}$$

We then substitute Eq. (59) into Eq. (53) and neglect the following terms. Assuming equal pumps $\tilde{\Lambda}_A=\tilde{\Lambda}_B=\tilde{\Lambda}$, we notice that $(C_{as}^A\tilde{\Lambda}_A+C_{as}^B\tilde{\Lambda}_B)\ll(C_{nn}^A\tilde{\Lambda}_A+C_{nn}^B\tilde{\Lambda}_B)$ due to $C_{as}^A\approx -C_{as}^B$. Furthermore, when the lasers are unlocked, terms involving relative phases $\psi_{sa}(t)$ are negleted in the random phase approximation. Inside the lockband, where $\psi_{sa}=$const, numerical analysis shows that either $\tilde{E}_a$ or $\tilde{E}_s$ vanishes. In either case terms of the type $\tilde{E}_a\tilde{E}_s\sin(\psi_{sa})$ can be dropped. The resulting class-*A* equations for the intensities $\tilde{I}_n=\tilde{E}_n^2$ of the composite-cavity eigenmodes are

$$\dot{\tilde{I}}_a=(\xi_a-\beta_a\tilde{I}_a-\theta_{as}\tilde{I}_s)\tilde{I}_a, \tag{62}$$

$$\dot{\tilde{I}}_s=(\xi_s-\beta_s\tilde{I}_s-\theta_{sa}\tilde{I}_a)\tilde{I}_s. \tag{63}$$

Because we chose to keep population pulsations, our class-*A* equations are valid for equally pumped lasers operating near threshold. Equations (62) and (63) clearly describe a competition between the two modes [54,14] and are equivalent to the equations describing dynamics of two species competing for the same source of food [67]. For the *n*th mode, the net gain is

$$\xi_n=2\gamma\left(C_{nn}^2\mathcal{L}(\nu_n)\tilde{\Lambda}-\frac{\gamma_n}{\gamma}\right), \tag{64}$$

and the self-saturation coefficient is

$$\beta_n=2\gamma C_{nn}\mathcal{L}^2(\nu_n)\tilde{\Lambda}\,[(C_{nn}^A)^2+(C_{nn}^B)^2]. \tag{65}$$

The cross-saturation coefficient for the *n*th mode saturated by the *m*th mode,

$$\theta_{nm}=\theta_{nm}^{hb}+\theta_{nm}^{pp}, \tag{66}$$

contains a spatial hole burning part

$$\theta_{nm}^{hb}=2\gamma C_{nn}\mathcal{L}(\nu_n)\mathcal{L}(\nu_m)\tilde{\Lambda}(C_{nn}^AC_{mm}^A+C_{nn}^BC_{mm}^B), \tag{67}$$

and a population pulsation part

$$\theta_{nm}^{pp}=\gamma C_{nn}\mathcal{L}(\nu_m)\tilde{\Lambda}[(C_{nm}^A)^2+(C_{nm}^B)^2]\mathcal{D}_{nm}[w(\alpha_m d_{nm}+1)-v_{nm}(\alpha_m-d_{nm})]. \tag{68}$$

As it was recognized in Ref. [54] (Sec. 9-2), the behavior of a two-mode laser strongly depends on the coupling parameter

$$\mathcal{C}=\frac{\theta_{as}\,\theta_{sa}}{\beta_a\,\beta_s}, \tag{69}$$

and on the effective gains

$$\xi_a'=\xi_a-\frac{\theta_{as}}{\beta_s}\xi_s\quad\text{and}\quad\xi_s'=\xi_s-\frac{\theta_{sa}}{\beta_a}\xi_a. \tag{70}$$

Here are the stable, positive intensity, fixed points of Eqs. (62) and (63) [54]. If $\xi_s'<0$ and $\xi_a>0$, then

$$\tilde{I}_a=\frac{\xi_a}{\beta_a}\quad\text{and}\quad\tilde{I}_s=0, \tag{71}$$

and if $\xi_a'<0$ and $\xi_s>0$, then

$$\tilde{I}_a=0\quad\text{and}\quad\tilde{I}_s=\frac{\xi_s}{\beta_s}. \tag{72}$$

For $\mathcal{C}<1$ and $\xi_a'>0$, and $\xi_s'>0$, we have

$$\tilde{I}_a=\frac{\xi_a'/\beta_a}{1-C}\quad\text{and}\quad\tilde{I}_s=\frac{\xi_s'/\beta_s}{1-C}. \tag{73}$$

Not all of these solutions can be stable at the same time. The two first stable fixed points (71) and (72) may coexist while the third fixed point (73) can be the only stable fixed point in the system. This can be understood in terms of the competition between the modes.

If the modes are strongly coupled, the cross-saturation coefficients θ_{nm} are big enough for both solutions, Eqs. (71) and (72), to be stable. Then, we speak of *strong mode competition* that allows for one winner only. The mode *n* which reaches the threshold first is the only survivor. The other mode *m*, even though it is pumped above threshold $\xi_m>0$, experiences negative effective gain ($\xi_m'<0$) due to the cross-saturation by the mode *n*, and will never rise above threshold. Strong mode competition is characterized by $\mathcal{C}>1$. When $\mathcal{C}<1$ we speak of *weak mode competition* that allows for the possibility of both modes to be above threshold (73). If one of the modes experiences more gain, it will oscillate with the higher amplitude but will never be able to depress the other mode. Lastly, note that in the weak competition case, one of the modes may experience $\xi_m'<0$ due to higher losses or by moving out of the gain profile. Then, the stable solution is Eq. (71) for the *n*th mode. The survivor is selected not via strong competition but simply due to the death of the competitor.

Our calculations show that including population pulsations is necessary to achieve strong competition between composite-cavity modes. The customary treatment neglects the phenomenon resulting in a complete lack of bistability in the locked solutions.

III. RESULTS

Our main objective is to study single-frequency synchronization (locking) between two coupled lasers. In this paper, lockband is defined as a range of (normalized) cavity length difference dL/λ within which the two lasers are locked to a single frequency. In terms of composite-cavity modes, the lasers are single-frequency locked when (i) only one

composite-cavity mode is above threshold as described by the solutions (71) and (72) or, (ii) when both composite-cavity modes are above threshold (73) and are frequency locked with $\psi_{sa}=$ const. There are other possibilities for synchronization (locking) which are not considered in this paper because they do not fall into the single-frequency locking category. Examples include synchronization of multimode lasers and situations involving instabilities leading to more complicated behavior and more general types of synchronization. This will be a subject of later publication dealing with coupled semiconductor lasers.

The results are presented in the form of lockbands in a two-dimensional parameter plane $(T, dL/\lambda)$. First, we focus on class A, and then, consider the transition from class-A to class-B lasers. Furthermore, we systematically study the dependence of the lockband on the carrier decay rate Γ_N, polarization decay rate Γ, pump $\tilde{\Lambda}$, and coupling mirror losses γ_M. To calculate the lockband, we use the bifurcation continuation package AUTO [62]. Under the variation of one parameter the transition between locked and unlocked laser operation is detected as a bifurcation, and is then continued in two parameters. This method is superior over the traditional approach which requires sampling of the entire parameter space by simulations [68]. All the numerical calculations in this section are performed using class-B Eqs. (53)–(55) (valid in class-B and class-A regime) for the pair of modes k_a and k_s. On the other hand, our class-A Eqs. (62) and (63) together with the analytical solutions (71)–(73) prove helpful by validating near threshold and providing physical explanation of the numerical results.

We set the length of cavity A to $L_A=1$ m, and the length of cavity B is $L_B=1\mathrm{m}+dL$. Furthermore, we use $\omega=(2\pi\times10^6)c$ and $\nu_k=\Omega_k$ in the formulas for $\mathcal{L}(\nu_k)$, α_k, d_{nm}, and $\mathcal{D}_{nm}$. After a close inspection of the analytical formulas for ξ_n, β_n, and θ_{nm} we decided to divide the numerical investigation into two parts. We start with large $\Gamma=1000$ GHz and then study the changes in the lockband as Γ decreases to a few GHz.

A. Rapid polarization decay

In Fig. 5 we show lockbands for zero losses in the coupling mirror. The dashed curve is obtained using class-A Eqs. (62) and (63), while the solid curves were obtained using class-B equations (53)–(55). In class-A equations a locked state continuously turns into an unlocked state via transcritical bifurcation (Ref. [69], p. 326). In class-B equations (solved in class-A regime), the locked state disappears along the solid curve and the system settles down to the remote unlocked state. This discontinuous transition between the stable states involves a narrow region of coexistence between locking and unlocking which is explained in Sec. III C.

For $\Gamma=1000\mathrm{GHz}\gg|\omega-\nu_{s(a)}|$, we can make the approximations $\mathcal{L}(\nu_n)\approx1$ and $\alpha_n\approx0$. Then, according to formulas (64)–(66), the lockband depends on the carrier decay rate Γ_N via $\mathcal{D}_{nm}$, on the pump $\tilde{\Lambda}$, and on the losses in the coupling mirror γ_M. Furthermore, if the coupling mirror is lossless, we expect the lockbands for the antisymmetric mode and for the symmetric mode to be almost identical.

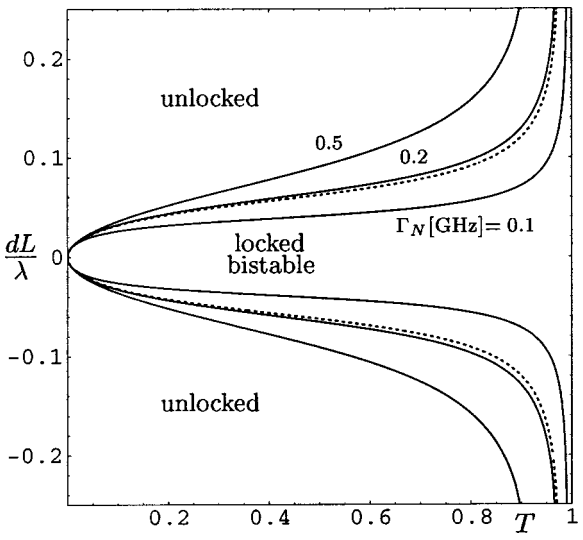

FIG. 5. Bistable lockband calculated using class-A equations (62) and (63) (dotted curve) for $\Gamma_N=0.2$ GHz and class-B equations (53)–(55) (solid curves) for $\Gamma_N=0.1$, 0.2, and 0.5 GHz. Other parameters are $\Gamma_E=0.01$ GHz, $\Gamma=1000$ GHz, $\gamma_M=0$, and $\tilde{\Lambda}=1.1$.

The lockbands in Fig. 5 are bistable which means that the parameter range where the lasers can lock at the frequencies of the antisymmetric and symmetric mode fully coalesce. Consequently, we see only one curve defining the transition from locking to unlocking. For the parameters inside the lockband, there exist two stable points and they have equal basins of attraction (equally large regions in the phase space with initial conditions leading to a given fixed point). Which fixed point the system settles to depend on the initial condition. Population pulsations and hole burning are necessary for the bistability to occur [54,14].

According to Eqs. (68) and (60) the coupling between the modes increases with Γ_N because of increasing population pulsation. Figure 5 indeed shows that the bistable lockband expands with increasing Γ_N. Figure 6 illustrates the dependence of the lockband on pump $\tilde{\Lambda}$. The expected result from a multimode theory with weak coupling between the modes is that subsequent modes reach threshold as pump increases. However, with strong mode competition one expects the laser to remain single mode. In our example of a two-mode laser system, coupling (competiton) between composite-cavity modes is enhanced with $\tilde{\Lambda}$ (Fig. 6). The bistable lockband widens with $\tilde{\Lambda}$ as in the early experiment from Ref. [15].

So far, all the lockbands we presented were fully bistable and almost symmetric with respect to $dL/\lambda=0$. Formulas for ξ_n, β_n, and θ_{nm} already suggest this type of symmetry, note that for long cavities considered here, $C_{aa}\approx C_{ss}$ and $C_{aa}^{A(B)}\approx C_{ss}^{B(A)}$. The asymmetry in the lockband may then be caused either by the different losses associated with the different modes or by the different detunings of the modes from the atomic frequency ω. We first focus on the influence of different cavity losses. The influence of detuning is discussed

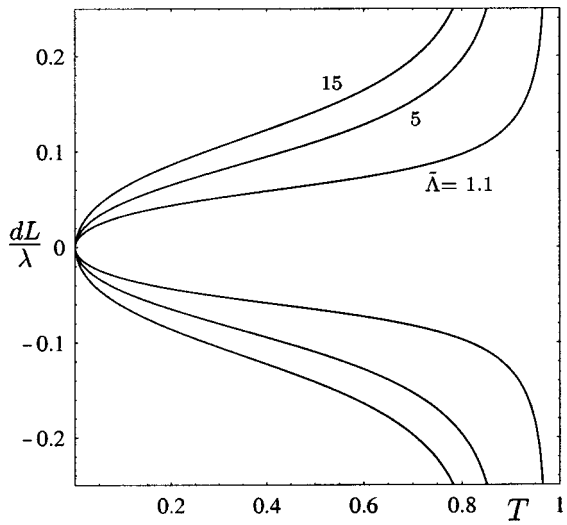

FIG. 6. Bistable lockband for different values of the pump $\tilde{\Lambda}$ while $\Gamma_E = 0.01$ GHz, $\Gamma_N = 0.2$ GHz, $\Gamma = 1000$ GHz, and $\gamma_M = 0$.

in the following section because it does not play any role for the large Γ considered here.

According to formula (42), different composite-cavity modes may experience different cavity losses if their amplitudes at the lossy coupling mirror are different. As can be seen in Fig 1(b), the antisymmetric mode amplitude at $z = 0$ is usually negligible while the symmetric mode amplitude at $z = 0$ can be as large as the amplitude of the mode itself. Hence, we expect the symmetric mode to experience higher cavity losses then the antisymmetric mode. The lockbands for different relative coupling mirror losses $\gamma_M = \Gamma_M / \Gamma_{out}$ are plotted in Figs. 7 and 8. The dotted curves represent the lossless coupling mirror and are included for reference. The key difference from the results shown in Figs. 5 and 6 is that, for nonzero γ_M, lockbands for different modes no longer coalesce.

At the low pump of $\tilde{\Lambda} = 1.1$, assuming barely 1% of the outcoupling losses in the coupling mirror already affects the bistable lockband [Fig. 7(b)]. As expected, the symmetric mode lockband shrinks with increasing γ_M, and almost disappears at $\gamma_M = 0.5$. On the other hand, the antisymmetric mode lockband expands asymetrically [Fig. 7(a)] because $u_s(0)$ is not a symmetric function of dL/λ. For $\gamma_M = 0.5$ in Fig. 7(a), the antisymmetric mode lockband extends into the region of large dL/λ where the mode competition is weak ($\mathcal{C} < 1$), and where two-mode operation is expected. There, we have an example of a single winner due to the death of the competitor, namely, the extra losses due to the absorption in the coupling mirror overcome the low gain and cause the symmetric mode to be below threshold.

When the lasers are pumped three times above threshold their ability to synchronize becomes more resistant to changes in γ_M. Small $\gamma_M = 0.01$ does not visibly influence the bistable lockband and deviations from the dashed curve appear at $\gamma_M = 0.1$. Figure 8(b) shows that the symmetric mode lockband starts shrinking at two places near $T = 0.9$ and $dL/\lambda = \pm 0.1$. As γ_M increases further it splits into three pieces. At $\gamma_M = 0.25$ [Fig. 8(b)], the lower piece is completely separated from the middle piece, and the upper piece is begining to detach. With further increase in γ_M, the side pieces disappear and the middle piece shrinks toward the origin of the $(T, dL/\lambda)$ plane.

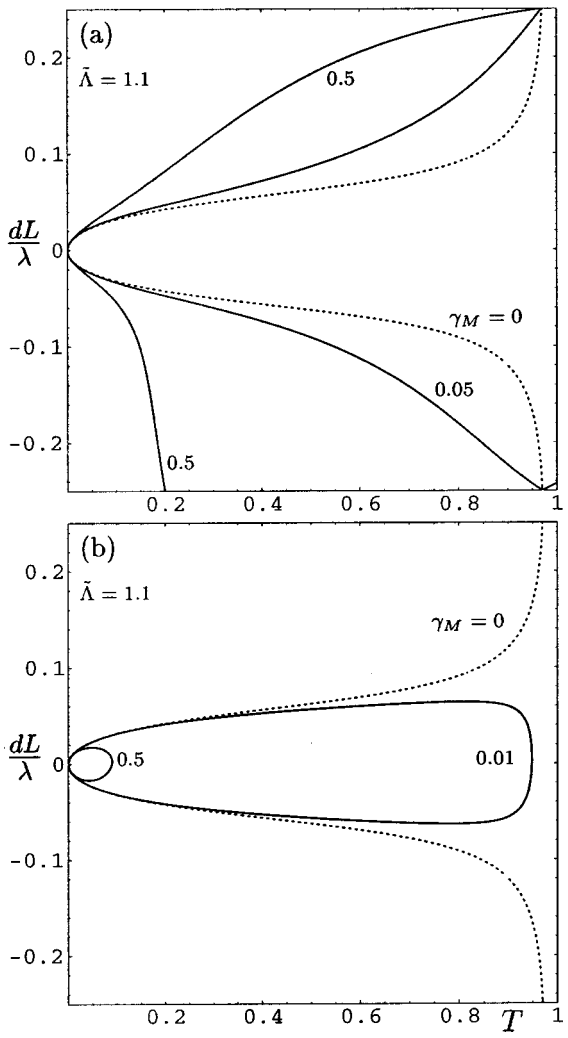

FIG. 7. Lockbands of the antisymmetric (a) and the symmetric (b) mode for different coupling mirror losses γ_M. The pump $\tilde{\Lambda} = 1.1$ and other parameters are as in Fig. 6.

The antisymmetric mode lockband widens slightly [Fig. 8(a)] but no longer extends to the region of weak mode coupling where $\mathcal{C} < 1$; compare with Fig. 7(a).

It is important to realize that losses in the coupling mirror not only affect the shape of the lockband in the parameter space as shown in Fig. 8. They also decrease the basin of attraction for the symmetric mode fixed point.

B. Slow polarization decay

When Γ decreases (due to decrease in $\Gamma_{dephase}$) to the value comparable with $|\omega - \nu_{s(a)}|$, the frequency pulling parameters α_n and the Lorentzians $\mathcal{L}(\nu_n)$ change with T and dL/λ and affect the mode competition. Furthermore, α_n and $\mathcal{L}(\nu_n)$ may change independently of T and dL/λ, for example, due to external magnetic field, changes in the cavity-length $L_A(L_B)$ or in the background refractive index. Here,

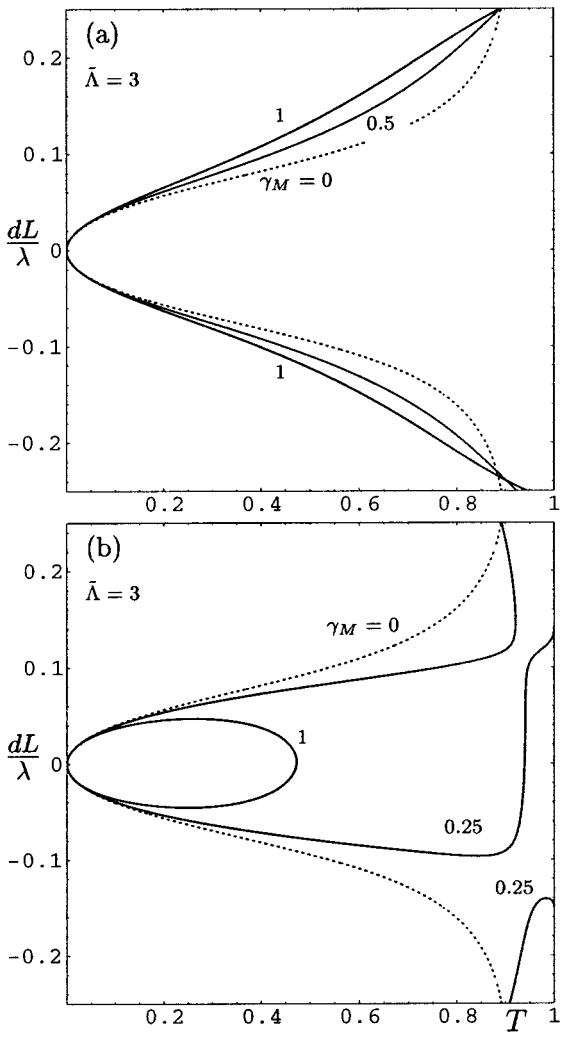

FIG. 8. Lockbands of the antisymmetric (a) and the symmetric (b) mode for different coupling mirror losses γ_M. The pump $\tilde{\Lambda} = 3$ and other parameters are as in Fig. 6.

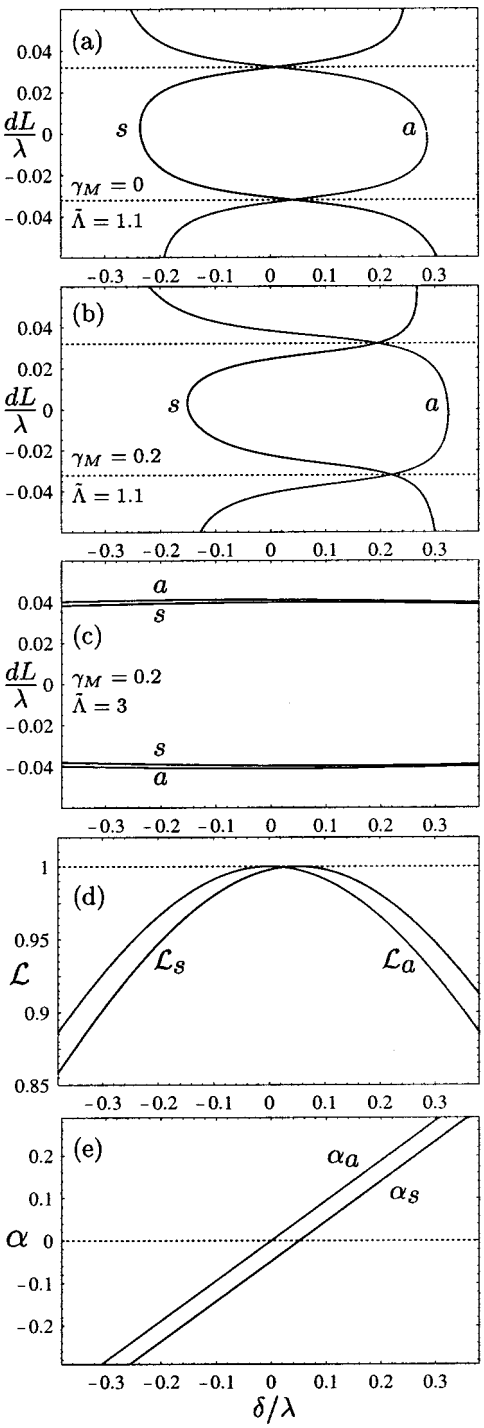

FIG. 9. Lockbands of the antisymetric a and the symetric s mode as a function of δ for fixed $T = 0.1$ [panels (a)–(c)]. Panel (d) shows the gain profiles corresponding to the two modes at $dL/\lambda = 0$, and panel (e) shows the corresponding frequency pulling parameters α_a and α_s at $dL/\lambda = 0$. Here, $\Gamma = 2$ GHz and other parameters are as in Fig. 6. The dotted curves are obtained for $\Gamma = 1000$ GHz.

in addition to scanning the $(T, dL/\lambda)$ plane, we choose to tune the frequencies of the modes by varying the lengths of the cavities on the fine scale of a fraction of the wavelength λ. Parameter δ is introduced to account for the difference from the cavity-A length of 1 m, and the cavity-B length of $(1m + dL)$. During calculations, $\delta = L_A - 1$ m and $dL = L_B - 1$ m $- \delta$ are the two independent parameters.

Let us fix the transmission T to 10%, decrease Γ from 1000 GHz to 2 GHz, and focus on Fig. 9. The dotted curves define the lockband for the case of large Γ and lossless coupling mirror. They show no variation for the range of δ shown in the figure because Lorentzians are unity and the frequency pulling parameters equal zero. However, when Γ is decreased, the Lorentzians and the α parameters vary as shown in Fig. 9(d)–9(e). These variations have substantial consequence on the lockband [Fig. 9(a)]. One bistable lockband splits into two such that the locking to the antisymmetric mode is more dominant for the negative values of δ and the locking to the symmetric mode is more dominant for the positive values of δ. Furthermore, each lockband is bounded on one side within the considered range of δ. Including losses in the coupling mirror makes the end of the antisymmetric-mode lockband expands toward positive δ, while the symmetric-mode lockband shrinks slightly [Fig. 9(b)]. This sensitive dependence on δ almost disappears

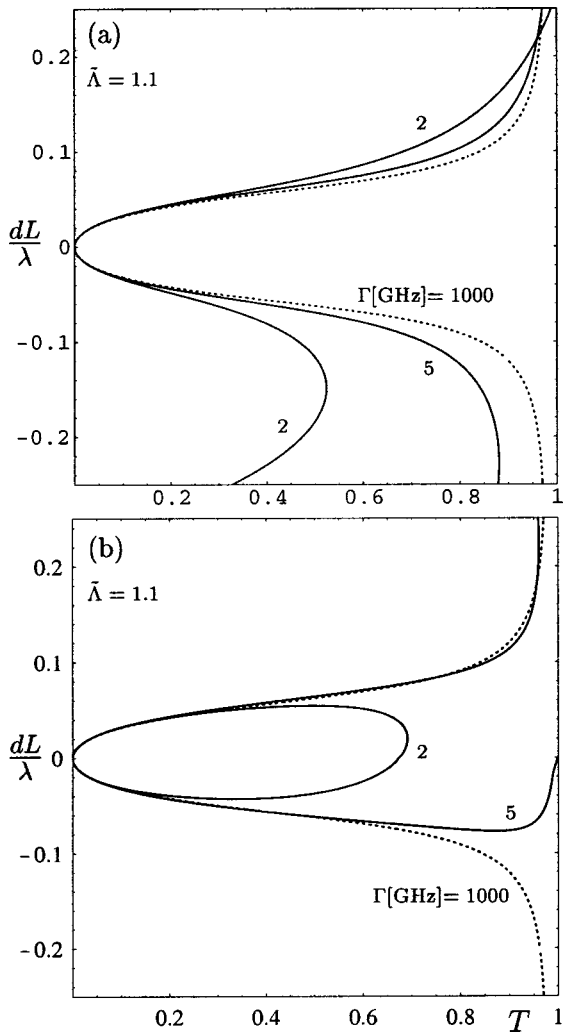

FIG. 10. Lockbands of the antisymmetric (a) and the symmetric (b) mode for different values of the polarization decay rate Γ. Other parameters are as in Fig. 6.

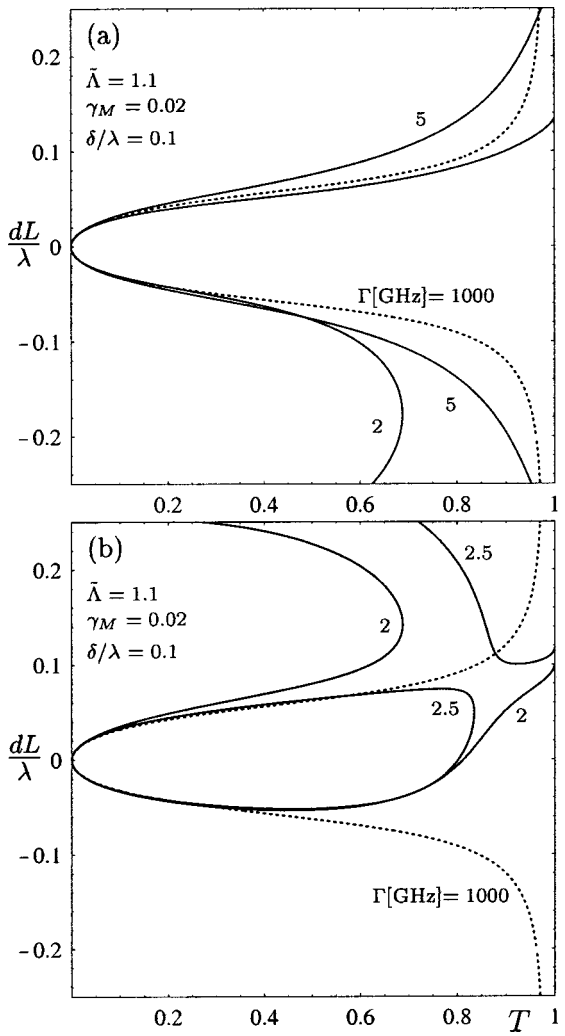

FIG. 11. Lockbands of the antisymmetric (a) and the symmetric (b) mode for different values of the polarization decay rate Γ in the presence of middle-mirror losses γ_M and cavity detuning δ. Other parameters are as in Fig. 6.

when the pump is increased to three times above threshold [Fig. 9(c)]. Actually, the lockband in [Fig. 9(c)] has similar shape to that in [Fig. 9(b)] but on the larger range of δ, to the extent where extra modes have to be included. A summary of how the lockbands are affected by the parameters of the coupled-cavity laser is provided in Figs. 10 and 11. In both figures Γ is decreased from 1000 GHz to a few gigahertz. We start with no losses in the coupling mirror (Fig. 10), then include $\gamma_M = 0.02$ and detune the cavities in the favor of the symmetric mode (Fig. 11). The antisymmetric and the symmetric mode lockbands almost overlap for $\Gamma > 10$ GHz. When Γ decreases to 5 GHz, the two lockbands differ visibly (Fig. 10). The effect of small Γ is similar to the effect of γ_M. The antisymmetric mode lockband again extends to the region of weak coupling [Fig. 10(a)] suggesting that the symmetric mode moves out of the gain profile [Fig. 10(b)]. Figure 2(a) already shows that, with increasing T, the symmetric mode becomes more detuned from ω than the antisymmetric mode.

Increasing the length of the lasers by $\delta/\lambda = 0.1$ has no effect on the lockband for $\Gamma > 5$ GHz. In particular, the symmetric mode lockband remains shrank due to coupling mirror losses. As Γ decreases below 5 GHz, the symmetric mode lockband expands toward the positive values of dL/λ as shown in Fig. 11(b). An additional piece of the symmetric mode lockband appears in the upper-right corner of the $(T, dL/\lambda)$ plane [Fig. 11(b)]. The two pieces of the symmetric lockband approach each other at $\Gamma \approx 2.5$ GHz and merge into one lockband [$\Gamma = 2$ GHz in Fig. 11(b)]. Here, the effect of δ overcomes the effect due to mirror losses and results in partialy restored symmetric mode lockband. The antisymmetric mode lockband, shown in Fig. 11(a), expands into the region of negative dL/λ.

Lastly, when the pump is increased to $\tilde{\Lambda} = 3$, the effects of $\gamma_M = 0.02$ and $\delta/\lambda = 0.1$ are small. Both lockbands are almost restored to the shape of the dotted curve.

C. Class *A* to class *B*

This section focuses on differences in the locking mechanisms between class-*A* and class-*B* lasers. Bifurcation theory

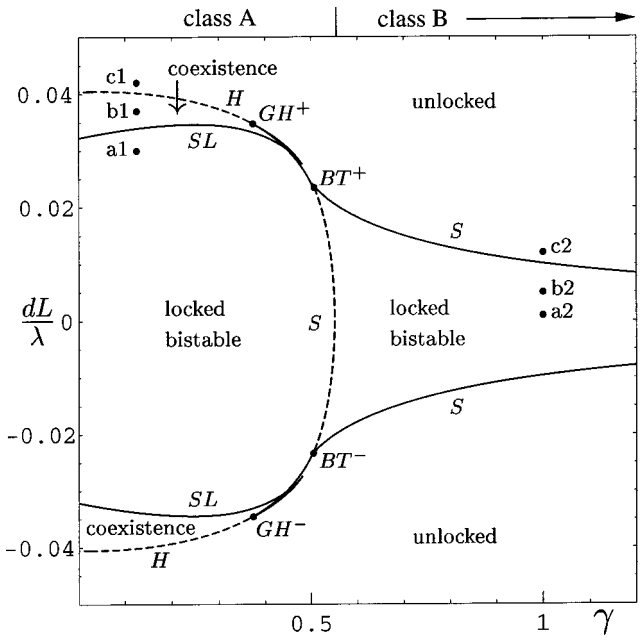

FIG. 12. Transformation of the lockband at $T=0.1$ as γ increases from class-*A* to class-*B* regime. The term "bistable" denotes the region with two stable fixed points, while "coexistence" denotes regions with two stable fixed points and one stable periodic orbit. *H* stands for Hopf, *S* for saddle-node of fixed points, and *SL* for saddle-node of limit cycle. The solid curves represent supercritical and the dashed curves represent subcritical bifurcations. The pump rate is $\tilde{\Lambda}=3$ and $\Gamma=10$ GHz.

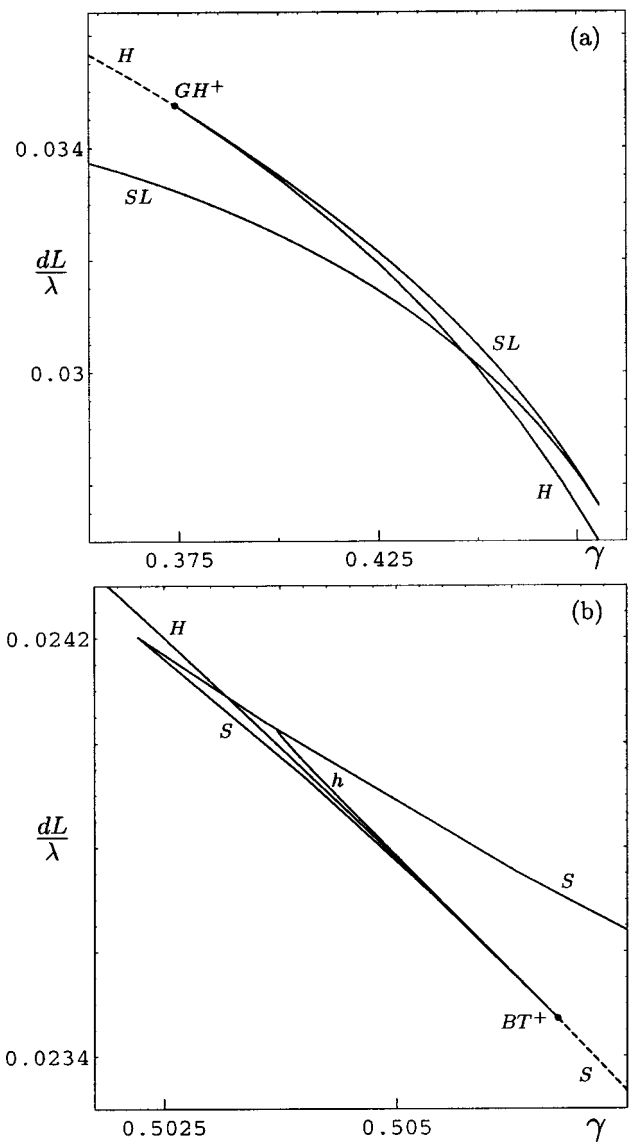

FIG. 13. Expended bifurcation diagram from Fig. 12 near the generalized Hopf point GH^+ (a) and the Bogdanov-Takens point BT^+ (b), respectively. In panel (b) *h* stands for homoclinic bifurcation

is used to identify qualitative changes (bifurcations) [69] in the phase space of the system at the locking-unlocking transition. In Fig. 12 bifurcations of stable solutions (called supercritical) are plotted as solid curves, and bifurcations of unstable solutions (called subcritical and needed for understanding the dynamical picture as they sometimes produce stable solutions too) are plotted as dashed curves. In the saddle-node bifurcation of fixed points denoted as *S*, two fixed points are created. In a Hopf bifurcation denoted as *H*, a fixed point bifurcates with a periodic orbit. In a generic saddle node of periodic orbit bifurcation *SL*, two periodic orbits are created.

It is important to note that, due to the symmetry between the modes, bifurcations of the symmetric and the antisymmetric mode fixed points nearly overlap. Therefore, each *S* and *H* curve in Fig. 12 actually indicates two bifurcations (of the two coexisting fixed points). Furthermore, the saddle node of periodic orbit bifurcation *SL* in Fig. 12 is close to a singular saddle node of periodic orbit bifurcation (also called subcritical pitchfork bifurcation) where an unstable orbit turns stable and two extra unstable orbits appear.

In Fig. 12, the lockband is bounded by (i) the supercritical parts of the *S* curve for $\gamma>0.5$ and (ii) either the *SL* curves or *H* curves for $\gamma<0.5$, due to hysteresis. The term *coexistence* denotes regions with two stable fixed points and a stable periodic orbit, while *bistable* denotes regions with two stable fixed points.

In the class-*A* regime ($\gamma<0.5$), a typical transition that occurs when dL/λ changes is depicted in the first column in Fig. 14. For the parameters within the lockband [Fig. 14(a1) and point a1 in Fig. 12] there exist two stable fixed points. They correspond to locking to either the antisymmetric or the symmetric mode. The antisymmetric (symmetric) mode fixed point of Eqs. (53)–(55) has a large amplitude of the antisymmetric (symmetric) mode but also a small contribution of the symmetric (antisymmetric) mode. Cross-saturation prevents this small contribution from becoming significant. The phases of the two modes are locked ($\dot{\psi}_{sa}=0$) so the lasers lase at the same frequency. Figure 14(a1) shows that, on top of the two fixed points, there exist an unstable periodic orbit (plotted in gray). As $|dL/\lambda|$ increases towards the border of the lockband, two extra periodic orbits are born, one of which is stable, in supercritical saddle-node of periodic orbit bifurcation *SL* [Fig. 14(b1) and point b1 in Fig 12]. The stable periodic orbit (plotted in black) represents the state of

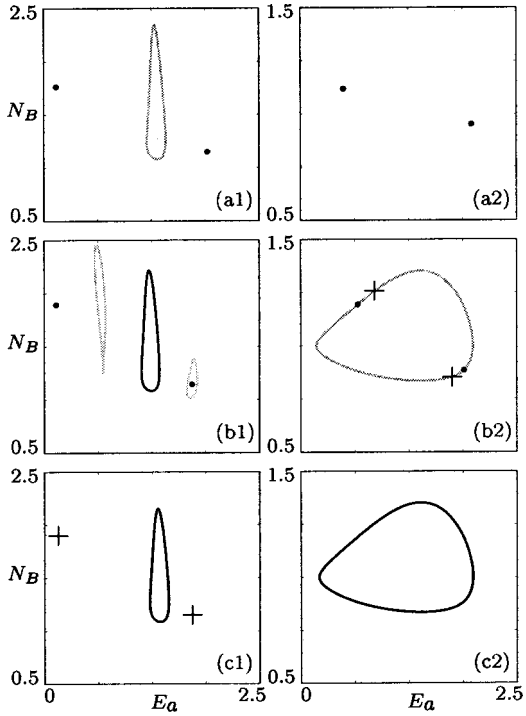

FIG. 14. Trajectories in the inversion N_B vs field amplitude E_a plane showing locking-unlocking transition in class-*A* lasers (column 1) and in class-*B* lasers (column 2). From (a1) to (c1) $\gamma = 0.125$ and $dL/\lambda = 0.03$, 0.037, and 0.042. From (a2) to (c2) $\gamma = 1$ and $dL/\lambda = 0.005$, 0.0095, and 0.011, as indicated in Fig. 12. The dots denote stable and the crosses denote unstable fixed points.

unlocked laser operation where both composite-cavity modes are above threshold and their phases drift apart [Fig. 15(a)]. In an experiment, and in most numerical analysis, the system settles to one of the stable fixed points and the appearance of the stable periodic orbit is usually unnoticed. As $|dL/\lambda|$ increases towards *H*, the two unstable orbits, plotted in gray in [Fig. 14(b1)], shrink onto the stable fixed points. At *H*, the two stable fixed points almost simultaneously turn unstable via subcritical Hopf bifurcation. The cross-saturation can no longer prevent multimode operation and the system makes a transition to the only stable state—the periodic orbit [Fig. 14(c1) and point c1 in Fig 12]. The lasers switch from locked operation to unlocked operation that shows no traces of the former stable fixed points [Fig. 15(a)]. For parameters above (below) the upper (lower) curve *H*, the lasers are unlocked. If one reverses direction and decreases $|dL/\lambda|$ the lasers remain unlocked until reaching the curve *SL*, where the stable orbit disappears and the systems move to one of the stable fixed points. Due to the hysteresis, the border separating locked and unlocked operation depends on the direction in which $|dL/\lambda|$ changes. Class-*A* lasers lock due to strong composite-mode competition.

As γ approaches the value 0.5 [Fig. 12], the *SL* curves meet the *H* curves at codimension-two generalized-Hopf points (Ref. [69] Sec. 8.3) GH^+ and GH^- [Fig. 13(a)], and the *H* curves meet the *S* curves at codimension-two Bogdanov-Takens points (Ref. [69] Sec. 8.4) BT^+ and BT^- [Fig. 13(b)]. In a generic scenario for a Bogdanov-Takens

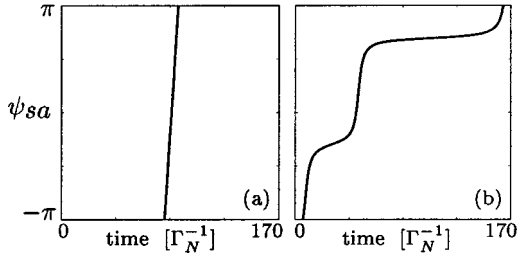

FIG. 15. Evolution of the phase difference for the laser-unlocked periodic orbit from Fig. 14(c1) [panel (a)] and the laser-unlocked periodic orbit from Fig. 14(c2) [panel (b)].

bifurcation, one expects an extra curve of homoclinic bifurcation where the period of the orbit born at *H* goes to infinity. This global bifurcation curve, marked as *h* in Fig. 13(b), was calculated using the HomCont part of AUTO [62]. It emerges from BT as expected, then joins *S* and continues along *S* for larger values of γ. In consequence, supercritical saddle-node bifurcations for $\gamma > 0.504$ take place on a periodic orbit.

Past BT^+ and BT^- one enters the regime of class-*B* lasers where the nature of the locking-unlocking transition changes significantly. In particular, the region of coexistence between locking and unlocking disappears and the lockband becomes narrower. For $\gamma = 1$ the lasers operate at the single composite-cavity mode only within $|dL/\lambda| < 0.0025$. As $|dL/\lambda|$ increases, the stable fixed points shift towards two composite-cavity mode operation where the modes are frequency locked ($\dot{\psi}_{sa} = 0$) [Fig. 14(a2) and point a2 in Fig. 12]. Near the border of, and still within, the lockband there is a saddle [crosses in Fig. 14(b2)] next to each stable fixed point. Furthermore, all four points are on an invariant circle formed by the unstable manifolds of the saddles. Along the supercritical branches of *S*, the saddles collide with the stable fixed points and disappear via saddle-node bifurcation. What remains is the stable periodic orbit corresponding to unlocked operation [Fig. 14(c2) and point c2 in Fig. 12]. Outside the lockband, the phase difference ψ_{sa} increases in time and, in contrast to class-*A* regime, shows ''ghosts'' of the stable fixed points [Fig. 15(b)]. Our analysis shows that moderately coupled class-*B* lasers lock due to frequency locking of the composite-cavity modes.

We would like to end our investigations by showing in Fig. 16 the entire lockband in class-*B* regime. Unlike in class-*A* regime (compare with Fig. 5), there are now two bifurcation curves, namely, saddle-node *S* and Hopf *H*. Furthermore, both curves become tangent at codimension-two saddle-node-Hopf points G^+ and G^- (Ref. [69], Sec. 8.5) where they change from supercritical to subcritical. The resulting lockband is bounded by the supercritical parts of *H* and *S* bifurcation curves. Generically, one expects other bifurcations to be created at G^+ and G^- that may lead to complicated dynamics and chaos (Ref. [69], Sec. 8.5). Those extra bifurcations will be studied in detail in the future publication.

IV. CONCLUSIONS

This paper describes a general theory of multimode coupled-cavity lasers that is based on a laser field expansion

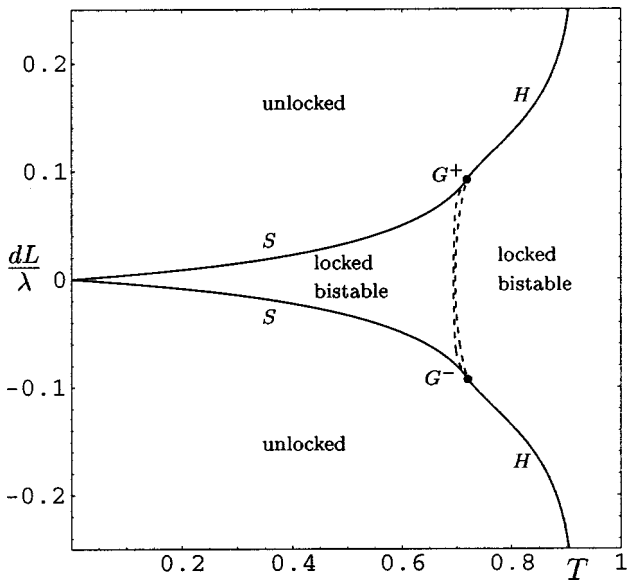

FIG. 16. Bistable lockband in class-*B* regime is bounded by the solid parts of the saddle-node *S* and the Hopf *H* curves which become tangent at saddle-node-Hopf points G^+ and G^-. Here, $\gamma = 2.5$ and $\tilde{\Lambda} = 3$. The solid curves represent supercritical and the dashed curves represent subcritical bifurcations.

in terms of composite-cavity eigenmodes. The theory is valid for all values of coupling and can be extended to any number of lasers. It accounts for nonlinear mode-coupling effects, coupling-mirror losses, and the dependence of the lasing frequencies on coupling. We derived the multimode coupled-laser equations and described their simplification by adiabatic elimination of the polarization and population equations (class-*B* and class-*A* lasers).

The full model consist of (i) differential equations for the time evolution of the slowly varying electric-field amplitude, phase, polarization, and population, as well as (ii) algebraic equations determining the composite-cavity eigenmodes. We extended previous studies by incorporating our system of differential algebraic equations into bifurcation continuation techniques. This allows for a systematic study of synchronization over an extensive parameter space.

First, we treated the class-*A* limit, which leads to the simplest form of the coupled-laser model. In this limit, the field intensity equations for the composite-cavity modes are equivalent to the equations describing competition of different species for the same source of food. Most importantly, the class-*A* equations allowed for derivation of analytical formulas describing laser locking in terms of competition between composite-cavity modes. In order to keep population pulsation effects, our class-*A* equations and resulting analytical expressions are restricted to low pump level. They validate near threshold and provide physical insight into the more general numerical results (which have no restriction on excitation level), helping to understand how the polarization decay rate, population difference decay rate, absorption in the coupling mirror and pump, influence the ability of coupled lasers to frequency lock. In particular, the class-*A* treatment reveales the importance of population pulsation which gives rise to bistable laser-locked solutions.

Second, we investigated the transition between class-*A* and class-*B* lasers and discovered a qualitative change in the nature of laser locking. Bifurcation theory was used to understand how strong composite-cavity mode competition, which is the laser-locking mechanism in class-*A* regime, gives way to frequency locking of the composite-cavity modes, the laser-locking mechanism in class-*B* regime. The results lay the foundation for a future investigation of coupled semiconductor lasers where the effects of inhomogeneous broadening and many-body interactions will have to be added to the theory presented in this paper.

ACKNOWLEDGMENTS

We thank J. Sieber and E. Basset for stimulating discussions. This work is supported in part by the U.S. Department of Energy under Contract No. DE–AC04–94AL8500 and the Alexander von Humboldt Foundation.

[1] T.H. Maiman, Nature (London) **187**, 493 (1960).
[2] N.G. Basov, E.M. Belenov, and V.D. Letokhov, Sov. Phys. Tech. Phys. **10**, 845 (1965).
[3] V.I. Perel and I.V. Rogova, Opt. Spectrosc. **25**, 401 (1968); **25**, 520 (1968).
[4] M.B. Spencer and W.E. Lamb, Jr., Phys. Rev. A **5**, 893 (1972).
[5] M. Phillip-Rutz, Appl. Phys. Lett. **26**, 475 (1975).
[6] W.W. Chow, Opt. Lett. **10**, 442 (1985).
[7] Y.C. See, S. Guha, and J. Falk, Appl. Opt. **20**, 1211 (1981).
[8] *Diode Laser Arrays*, edited by D. Botez and D. R. Scifres (Cambridge University Press, Cambridge, 1994).
[9] *High Power Multibeam Lasers and Their Phase Locking*, Proceedings of SPIE, edited by F. V. Lebedev and A. P. Napartovich (SPIE, Bellingham, WA, 1993) Vol. 2109.
[10] A.J. Fischer, K.D. Choquette, W.W. Chow, A.A. Allerman, D.K. Serkland, and K.M. Geib, Appl. Phys. Lett. **79**, 4079 (2001).
[11] P.W. Smith, Proc. IEEE **60**, 422 (1972).
[12] S.A. Shakir and W.W. Chow, Opt. Lett. **9**, 202 (1984).
[13] S.A. Shakir and W.W. Chow, Phys. Rev. A **32**, 983 (1985).
[14] W.W. Chow, IEEE J. Quantum Electron. **QE-22**, 1174 (1986).
[15] W.J. Fader, IEEE J. Quantum Electron. **QE-21**, 838 (1985).
[16] R.D. Li and T. Erneux, Phys. Rev. A **46**, 4252 (1992).
[17] R. Li and T. Erneux, Opt. Commun. **99**, 196 (1993).
[18] L. Fabiny, P. Colet, R. Roy, and D. Lenstra, Phys. Rev. A **47**, 4287 (1993).
[19] M. Silber, L. Fabiny, and K. Wiesenfeld, J. Opt. Soc. Am. B **10**, 1121 (1993).
[20] Y. Braiman, T.A.B. Kennedy, K. Wiesenfeld, and A. Khibnik, Phys. Rev. A **52**, 1500 (1995).
[21] R. Kuske and T. Erneux, Opt. Commun. **139**, 125 (1997).
[22] A.I. Khibnik, Y. Braiman, T.A.B. Kennedy, and K. Wiesenfeld, Physica D **111**, 295 (1998).
[23] M. Moller, B. Formann, and W. Lange, Quantum Semiclassic. Opt. **10**, 839 (1998).

[24] M. Moller, B. Formann, and W. Lange, Chaos, Solitons Fractals **10**, 825 (1999).
[25] V. Zehnle, Phys. Rev. A **62**, 033814 (1997).
[26] J.R. Terry, K.S. Thornburg, Jr., D.J. DeShazer, G.D. VanWiggeren, Shiqun Zhu, P. Ashwin, and R. Roy, Phys. Rev. E **59**, 4036 (1999).
[27] M. Moller, B. Formann, and W. Lange, J. Opt. B: Quantum Semiclassical Opt. **2**, 371 (2000).
[28] Z.P. Jiang and M. McCall, J. Opt. Soc. Am. B **10**, 155 (1993).
[29] R.D. Li and T. Erneux, Phys. Rev. A **49**, 1301 (1994).
[30] S.Y. Kourtchatov, V.V. Likhanskii, A.P. Napartovich, F.T. Arecchi, and A. Lapucci Phys. Rev. A **52**, 4089 (1995).
[31] V.P. Kandidov, A.V. Kondratev, and M.B. Surovitskii, Quantum Electron. **28**, 692 (1998).
[32] J. Tsacoyeanes, J. Appl. Phys. **64**, 32 (1988).
[33] G.C. Dente, C.E. Moeller, and P.S. Durkin, IEEE J. Quantum Electron. **26**, 1014 (1990).
[34] M.K. Chun, L. Goldberg, and J.F. Weller, Opt. Lett. **14**, 272 (1989).
[35] R.D. Li and T. Erneux, Phys. Rev. A **49**, 1301 (1994).
[36] A. Hohl, A. Gavrielides, T. Erneux, and V. Kovanis, Phys. Rev. Lett. **78**, 4745 (1997).
[37] J. Garcia-Ojalvo, J. Casademont, M.C. Torrent, C.R. Mirasso, and J.M. Sancho, Int. J. Bifurcation Chaos Appl. Sci. Eng. **9**, 2225 (1999).
[38] J. Mulet, C. Masoller, and C.R. Mirasso, Phys. Rev. A **65**, 063815 (2002).
[39] E. Kapon, J. Katz, A. Yariv, Opt. Lett. **10**, 125 (1984).
[40] W.W. Chow, J. Opt. Soc. Am. B **4**, 324 (1987).
[41] H.G. Winful and S.S. Wang, Appl. Phys. Lett. **53**, 1894 (1988).
[42] H.G. Winful, Phys. Rev. A **46**, 6093 (1992).
[43] H.G. Winful, S. Allen, and L. Rahman, Opt. Lett. **18**, 1810 (1993).
[44] P. Ru, P.K. Jakobsen, J.V. Moloney, and R.A. Indik, J. Opt. Soc. Am. B **10**, 507 (1993).
[45] L. Rahman and H.G. Winful, IEEE J. Quantum Electron. **30**, 1405 (1994).
[46] W. W. Chow, S. W. Koch, and M. Sargent III, *Semiconductor-Laser Physics* (Springer-Verlag, Berlin, 1997).
[47] S.S. Wang and H.G. Winful, Appl. Phys. Lett. **52**, 1774 (1998).
[48] G. Kozyreff, A.G. Vladimirov, and P. Mandel, Phys. Rev. Lett. **85**, 3809 (2000).
[49] H.G. Winful and L. Rahman, Phys. Rev. Lett. **65**, 1575 (1990).
[50] R. Roy and K.S. Thornburg, Jr., Phys. Rev. Lett. **72**, 2009 (1994).
[51] G.D. VanWiggeren and R. Roy, Science **279**, 1198 (1997).
[52] K.S. Thornburg, Jr., M. Moller, R. Roy, T.W. Carr, R.D. Li, and T. Erneux, Phys. Rev. E **55**, 3865 (1997).
[53] R. Oliva and S.H. Strogatz, Int. J. Bifurcation Chaos Appl. Sci. Eng. **11**, 2355 (2001).
[54] M. Sargent III, M. O. Scully, and W. E. Lamb, Jr., *Laser Physics* (Addison-Wesley, New York, 1974).
[55] A.A. Duarte and H.G. Solari, Phys. Rev. A **58**, 614 (1998).
[56] A.A. Duarte and H.G. Solari, Phys. Rev. A **64**, 033803 (2001).
[57] J. Sieber, SIAM J. Appl. Dyn. Sys. **1**, 248 (2002).
[58] U. Bandelow, M. Wolfrum, J. Sieber, and M. Radziunas, IEEE J. Quantum Electron. **QE-37**, 183 (2001).
[59] C.R. Mirasso, M. Kolesik, M. Matus, J.K. White, and J.V. Moloney, Phys. Rev. A **65**, 013805 (2001).
[60] A. Hohl and A. Gavrielides, Phys. Rev. Lett. **82**, 1148 (1999).
[61] S. Wieczorek, T.B. Simpson, B. Krauskopf, and D. Lenstra, Phys. Rev. E **65**, 045207(R) (2002).
[62] E. Doedel, T. Fairgrieve, B. Sandstede, A. Champneys, Yu. Kuznetsov, and X. Wang, http://sourceforge.net/projects/auto2000/
[63] W.A. Hamel and J.P. Woerdman, Phys. Rev. A **40**, 2785 (1989).
[64] A. E. Siegman, Proc. SPIE **4436**, 1 (2001).
[65] F.T. Arecchi, R. Meucci, G. Puccioni, and J. Tredicce, Opt. Commun. **51**, 308 (1984).
[66] W. W. Chow and S. W. Koch, *Sconductor-Laser Fundamentals* (Springer-Verlag, Berlin, 1999).
[67] A. D. Bazykin, *Nonlinear Dynamics of Interacting Populations*, World Scientific Series on Nonlinear Science A 11 (World Scientific, Singapore, 1998).
[68] B. Krauskopf in *Fundamental Issues of Nonlinear Laser Dynamics*, edited by Bernd Krauskopf and Daan Lenstra, AIP Conf. Proc. 548 (AIP, Melville, NY, 2000).
[69] Yu. A. Kuznetsov, *Elements of Applied Bifurcation Theory* (Springer, New York, 1995).